

Sim-to-real for high-resolution optical tactile sensing: From images to 3D contact force distributions

Carmelo Sferrazza and Raffaello D'Andrea¹

Abstract—The images captured by vision-based tactile sensors carry information about high-resolution tactile fields, such as the distribution of the contact forces applied to their soft sensing surface. However, extracting the information encoded in the images is challenging and often addressed with learning-based approaches, which generally require a large amount of training data. This article proposes a strategy to generate tactile images in simulation for a vision-based tactile sensor based on an internal camera that tracks the motion of spherical particles within a soft material. The deformation of the material is simulated in a finite element environment under a diverse set of contact conditions, and spherical particles are projected to a simulated image. Features extracted from the images are mapped to the 3D contact force distribution, with the ground truth also obtained via finite-element simulations, with an artificial neural network that is therefore entirely trained on synthetic data avoiding the need for real-world data collection. The resulting model exhibits high accuracy when evaluated on real-world tactile images, is transferable across multiple tactile sensors without further training, and is suitable for efficient real-time inference.

I. INTRODUCTION

Research on vision-based (or optical) tactile sensors aims to provide robots with high-resolution information about contact with external objects. However, while the images stemming from the various optical tactile sensing principles are intuitive and to some extent interpretable by human observations, the extraction of accurate physical quantities is challenging. In this regard, the complexity of mapping the information extracted from the images to the corresponding contact conditions mainly results from the fact that accurate modeling techniques for soft materials are generally not suitable for real-time applications. Additionally, previous research has predominantly focused on the estimation of low-dimensional quantities (e.g., total contact force, center of contact), which may be sufficient for a limited range of tasks, but not for generic applications, as is the case for tasks that involve arbitrary points of contact.

The work discussed in this article targets both these topics, proposing a data-driven approach to reconstruct the three-dimensional distribution of the contact forces applied to the soft surface of a vision-based tactile sensor. The sensing strategy was presented in the authors' previous work [1] and is based on the tracking of particles randomly spread within a soft gel. The use of data bypasses the need for modeling techniques with real-time guarantees, but as opposed to

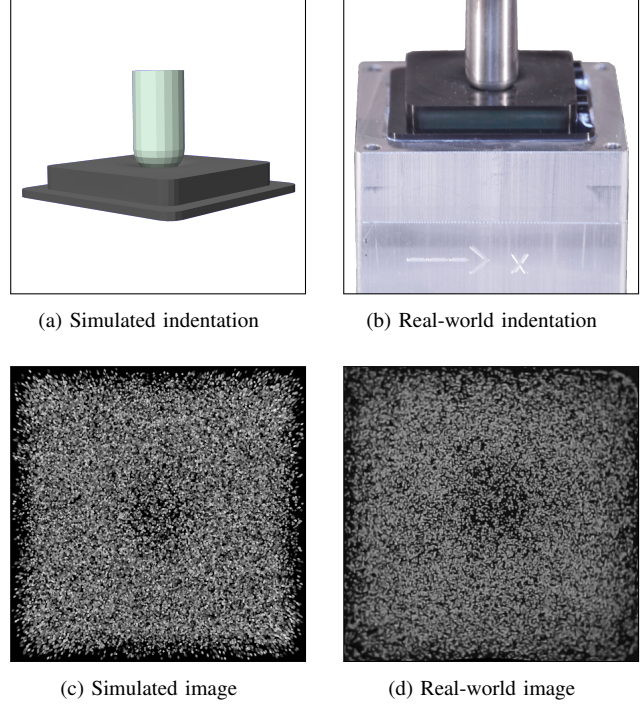


Fig. 1: This work builds upon the generation of training images in simulation for a data-driven, vision-based tactile sensor based on the tracking of a spread of particles.

classical data-driven strategies, here the data necessary for training the learning architecture at the core of the method are entirely generated in simulation. Furthermore, the estimation of the contact force distribution directly yields both the total contact force (i.e., the component-wise integral of the force distribution) and the contact locations (i.e., the surface patches where the contact pressure is nonzero), and is additionally suitable to represent generic contact conditions with arbitrary points of contact, therefore providing high versatility across several tasks.

The main contributions of this work are the following:

- It details a method to simulate the images captured by a vision-based tactile sensor [1], starting from simulations based on the finite element method [2] (FEM).
- It outlines two strategies to generate simulated datasets comprising tactile image features and labels. These strategies differ from the one presented in the authors' previous work [3], as they relax a small deformation assumption and simplify the transfer from simulation to reality. The datasets collected for this work comprise

^{*}This work was not supported by any organization
The authors are with the Institute for Dynamic Systems and Control, ETH Zurich, 8092 Zurich, Switzerland.
Correspondence to: csferrazza@ethz.ch

a variety of contact conditions, producing high shear and pressure forces with indenters of different shapes and sizes.

- It describes a tailored learning architecture, based on u-net [4], which can be trained entirely with simulated data. Besides yielding high accuracy when evaluated on real-world data, the entire pipeline can run in real-time up to a speed of 120 Hz.

A. Related work

In recent years, a number of tactile sensing principles [5] have been developed to address the needs of the robotics community. Among these, vision-based tactile sensors [6] employ standard cameras [7] or optical devices [8], [9] to infer the deformation of a soft membrane and obtain information about the contact with external objects that causes the deformation. This category of tactile sensors generally benefits from high resolution and ease of wiring, and its straightforward manufacture enables fast prototyping for robotic systems. Although the bulkiness of their sensing unit is the main limitation of such approaches, recent works have proposed compact solutions that exploit embedded cameras [10]–[12] or mirrors [13].

The sensory feedback provided by tactile sensors typically requires further processing, as it does not directly translate to the physical quantities of interest for robotic tasks. In this regard, model-based methods [14], [15] often rely on strong modeling assumptions (e.g., linear elasticity of the materials) to solve the processing task in an approximate fashion, while data-driven methods [16]–[18] aim to compute offline a mapping from raw data to the quantities of interest, in order to preserve accuracy while ensuring real-time inference.

While most of the literature has primarily focused on the estimation of low-dimensional physical quantities (e.g., total forces), recently several works have shifted the focus towards the estimation of distributed quantities, which aim to provide high-resolution tactile fields for a wide range of tasks. In the context of vision-based sensors, the estimation of the contact patches [15] has been proposed, and the reconstruction of the contact force distribution has been discussed, both in a model-based [14] and a data-driven [16] fashion. Additionally, various approaches have been proposed outside the vision-based domain, with regard to the estimation of the deformation field [19] and the pressure distribution [20].

As a result of the possibility of collecting and generating accurate data offline, data-driven approaches generally exhibit smaller estimation errors than model-based methods [8]. However, their bottleneck often lies in the fact that they require large amounts of training data and they do not often generalize well when employed in unseen contact conditions. In order to address the issue of data efficiency, a number of works have focused on generating training data in simulation to extract a model that retains its accuracy when employed in the real world. Examples of such sim-to-real (or sim2real) transfers can be found in the literature for edge prediction [21] and the estimation of the contact pressure [20] and the

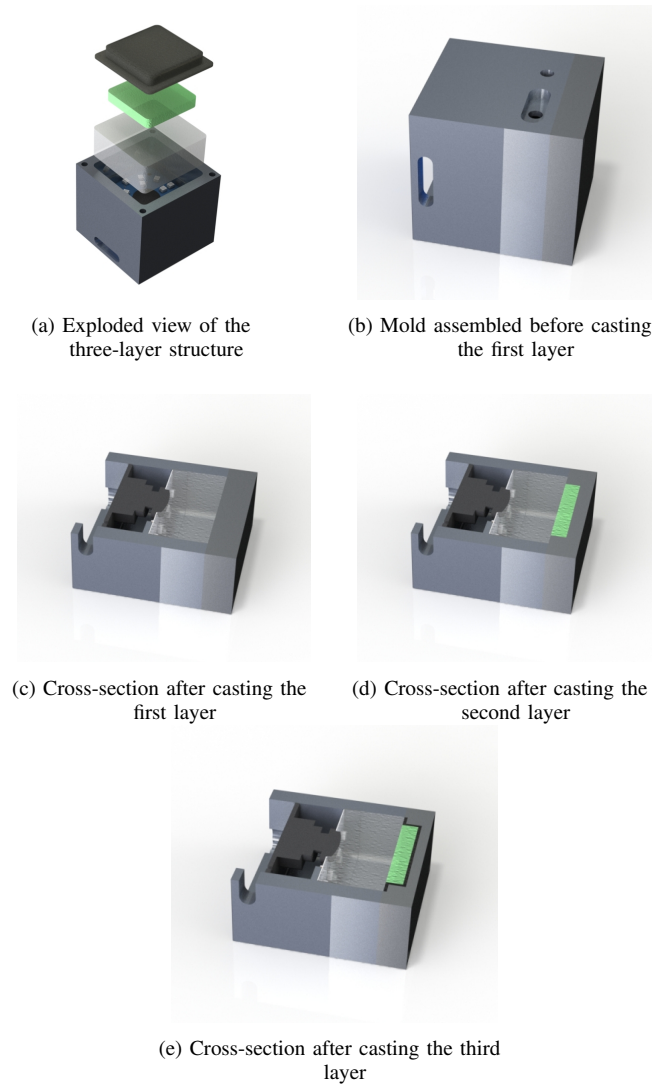


Fig. 2: The figure details the sensor’s fabrication. The soft materials are arranged in a three-layer structure (see (a)) on top of the camera and the LEDs, and were poured into the mold from the side, through lateral cavities such as those shown in (b). Three different lids (see (c)–(e)) were employed for each of the soft layers.

deformation field [22], [23]. In previous work, a sim-to-real approach was presented to estimate the 3D force distribution [3] for a limited range of scenarios.

This article presents two different methods to generate a dataset to train a data-driven approach entirely via FEM simulations, with the aim to reconstruct the three-dimensional contact force distribution applied to a vision-based tactile sensor. Image features were extracted from the tactile images generated in simulation, and mapped to three matrices representing the components of the force vectors applied over the soft sensing surface. The mapping was obtained via a tailored neural network architecture, which is able to capture various contact conditions as high shear and pressure forces, as well as indentations with flat or round objects. Additionally, high accuracy was retained on real-world data and the real-time speed could be more than doubled compared to previous work [3].

B. Outline

The sensing strategy and the hardware are described in Section II, while the method to generate tactile images and extract the related features is presented in Section III. Starting from the generated dataset, Sections IV and V describe the learning pipeline and the evaluation on simulated and real-world data, respectively. Final remarks and an outlook are included in Section VI.

II. HARDWARE

The tactile sensor employed in this work is based on a camera that tracks particles randomly distributed within a deformable material [1]. The soft materials are arranged in three layers, as shown in Fig. 2(a), and were poured (after degassing in a vacuum chamber) on top of the camera (ELP USBFHD06H with a fisheye lens) and the surrounding LEDs with the mold lying on one side, i.e., with the camera pointing sideways, as shown in Fig. 2(b). The fabrication strategy followed previous work [1], but it is presented extensively here to provide additional details for reproducibility:

- 1) A first layer of Elastosil® RT 601 RTV-2 (mixing ratio 7:1, shore hardness 45A) was poured into the mold, closed with a first lid (see Fig. 2(c)). The mold was then placed into an oven at 80 °C for 20 minutes for curing. This layer serves as a stiff base and facilitates light diffusion.
- 2) A release agent (Mann Ease Release™ 200) was sprayed before assembling the second lid, shown in Fig. 2(d). Then, a layer of Ecoflex™ GEL (mixing ratio 1:1, very soft, with shore hardness 000-35), mixed with green, fluorescent spherical particles (with a diameter of 150 to 180 μm), was poured into the mold. The mold was finally placed into an oven at 60 °C for 20 minutes for curing.
- 3) Finally, a layer of Elastosil® RT 601 RTV-2 (mixing ratio 25:1, shore hardness 10A), mixed with black silicone color (Elastosil® Color Paste FL), was poured into the mold, closed with a third lid, shown in Fig. 2(e). The mold was then placed into an oven at 80 °C for 45 minutes for curing. This layer is stiffer than the Ecoflex GEL, and shields the sensor from damage and light disturbances.
- 4) After removing the last lid, the sensor was placed back in the oven at 60 °C for 8 hours. This step has been shown to reduce stiffening caused by the aging of the materials [16].

The two soft upper layers amount to a rectangular prism of $32 \times 32 \times 6$ mm. The Ecoflex GEL and the black Elastosil layer have both been characterized previously [16] as hyperelastic materials using second-order Ogden models [24]. Given the large difference in hardness, the stiff base layer was considered rigid [16] in the FEM simulations discussed in the next sections.

III. DATASET GENERATION

Supervised learning is a natural data-driven way of processing sensory feedback and mapping raw data to the

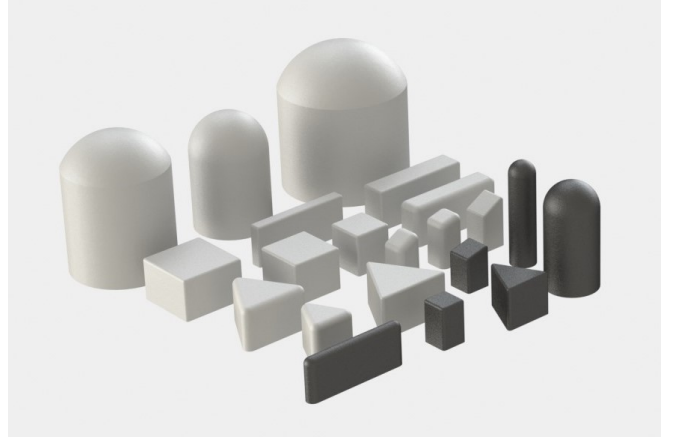


Fig. 3: The figure shows the indenters used to collect the training data in the FEM simulations. Real-world realizations of the black indenters were used to collect the test data in reality. Note that the indentation surfaces corresponds to the top surfaces in the figure. The sharp corners of the indenters were smoothed out to avoid a known singularity in the flat punch indentation experiment [25].

quantities of interest. In the context of vision-based tactile sensing, formulating the task in a supervised learning manner involves two crucial preliminary steps: I) the choice of appropriate features to condense the information contained in the images; II) the formalization of finite-dimensional labels representing the quantities of interest. Additionally, the availability of data necessary to train suitable learning architectures needs to be considered when addressing the formulation of the problem. In this work, training data were generated entirely in a finite element simulation environment with the objective of avoiding real-world data collection and maximizing the variability of the contact conditions without the need for complex hardware setups. A further advantage of collecting contact data in simulation is the possibility of extracting high-resolution tactile fields [16], which are otherwise not possible to measure with the commercially available commodity sensors. This work aimed to estimate the three-dimensional force distribution, which is a condensed representation of several contact quantities. In fact, the force distribution encodes both the contact locations, which can be obtained by thresholding the normal component, and the total contact forces, which can be obtained by integrating the distribution over the sensing surface. As opposed to the deformation field, the contact patches are exactly encoded in the force distribution, while the deformation field can, for example, show deformation also where no contact is applied, as a result of the elasticity of the soft material. Additionally, from the force distribution it is possible to compute the torques acting on the contact object, and all these properties remain valid for contact with multiple or arbitrary objects.

Two training datasets were built by performing indentations in an FEM simulation environment with the 21 different indenters shown in Fig. 3. The indentation trajectories were performed by either moving the indenter vertically and then purely horizontally, or by prescribing indenter motions from different angles followed by random perturbations in the

vicinity of the first indentation. A total of 2700 indentation trajectories (each comprising 50 indentation steps) were executed in simulation, with total forces up to 12 N in the vertical direction and up to 4 N in each of the horizontal directions. For each step of these trajectories, the contact force distribution and the displacement field were extracted at the nodes of a mesh refined around the contact between the indenter and the soft material. These quantities were further processed to compose two sets of features and labels, as described in Section III-A for the displacement field and Section III-B for the force distribution. Since the training dataset was entirely generated in simulation, two test datasets were collected in reality as described in Section III-C to verify the sim-to-real transfer and the real-world performance.

A. Training features

In this article, two different methods to extract image features are compared. The resulting types of features are denoted in the following as optical flow features and raw features, respectively. The starting points of both methods are the images captured by the internal camera, and for training purposes, these images were entirely generated in simulation. The soft materials were modeled in the FEM simulations as described in Section II. Highly accurate models were obtained for the same materials via state-of-the-art characterization experiments in previous work [16], where these models were also validated against a force-torque sensor. The Ogden model parameters used there were also employed in this work. A static friction coefficient of 0.45 was used, as it proved accurate for the indenters employed.

A gel coordinate system (see Fig. 5(a)) was defined by placing the origin at one of the bottom corners of the layer containing the particles, the z axis pointing towards the upper surface, and the x and y axes aligned with two of the horizontal edges. For each indentation step performed in simulation, the FEM provides the displacement field of the soft layer that comprises the particles. This displacement field is provided at the discrete nodes of the FEM mesh. For such nodes, also the initial position (at rest, before deformation) is known. In order to generate the dataset, a random distribution of particles was sampled for each indentation step, and an inverse distance weighted scheme [26] was used to interpolate the displacement field at the corresponding particle location s_j^G , for $j = 0, \dots, N_p - 1$, where N_p is the number of particles and the superscript G indicates the gel coordinate system. The 3D displacement of the j -th particle is denoted in the following as Δs_j^G . The strategy followed was to project the particles to the image plane using an ideal pinhole camera model [27], and only account for the camera's non-idealities at a later stage [3], as described in Section III-C. Therefore, as depicted in Fig. 5, the position s_j^G and the respective displacement Δs_j^G were first transformed from the gel coordinate system to the 3D pinhole camera coordinate system (indicated by

the superscript P) as

$$s_j^P = R^{GP} s_j^G + t^{GP}, \quad (1)$$

$$\Delta s_j^P = R^{GP} \Delta s_j^G \quad (2)$$

where the rotation matrix R^{GP} and the translation vector $t^{GP} := (t_x^{GP}, t_y^{GP}, t_z^{GP})$ are the pinhole camera's extrinsic parameters. These parameters could be chosen arbitrarily, but they were actually chosen to be close to the real-world camera's extrinsic parameters, as discussed in Section III-C. The pinhole image resolution was arbitrarily set to be 440×440 pixels, and although the focal length could also be chosen arbitrarily in this step, in order to exactly capture the region where the particle layer (which has a square horizontal section of 30×30 mm) is visible, this was set for both the image coordinates as

$$f := \frac{440}{30} t_z^{GP}. \quad (3)$$

The projection of the spherical particle centered at $s_p^P := (x_p^P, y_p^P, z_p^P)$ via the pinhole camera model results in an ellipse on the image plane [28], see Fig. 4(a). The pixel length r of the major axis of each ellipse can be computed via the projection formulas in the plane containing the camera's optical axis and the camera ray passing through the center of the spherical particle. An example projection in this plane is shown in Fig. 4(b). The coordinate \tilde{x}_p^P can be computed from the horizontal coordinates of the center of the particle as,

$$\tilde{x}_p^P = \sqrt{(x_p^P)^2 + (y_p^P)^2}. \quad (4)$$

Then, from the figure, it follows that:

$$\alpha = \arctan \left(\frac{z_p^P}{\tilde{x}_p^P} \right), \quad (5)$$

$$\beta = \arcsin \left(\frac{R}{\sqrt{(\tilde{x}_p^P)^2 + (z_p^P)^2}} \right), \quad (6)$$

$$\gamma = \alpha - \beta, \quad (7)$$

where R is the radius of the sphere. The pixel length r of the major axis can then be computed as:

$$\tilde{x}_r^P = \tilde{x}_p^P + R \sin \gamma, \quad (8)$$

$$z_r^P = z_p^P - R \cos \gamma, \quad (9)$$

$$\tilde{x}_l^P = \tilde{x}_p^P - R \sin(\gamma + 2\beta), \quad (10)$$

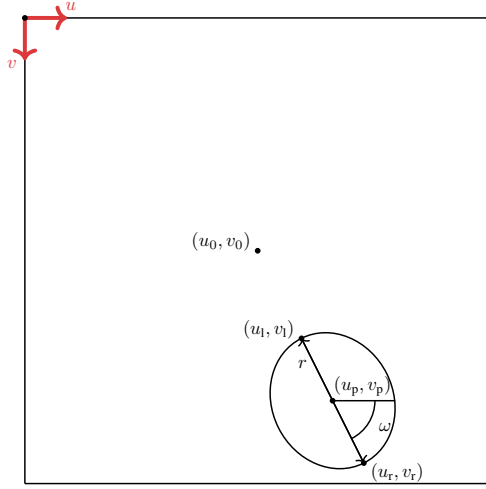
$$z_l^P = z_p^P + R \cos(\gamma + 2\beta), \quad (11)$$

$$r = \left| f \left(\frac{\tilde{x}_r^P}{z_r^P} - \frac{\tilde{x}_l^P}{z_l^P} \right) \right|. \quad (12)$$

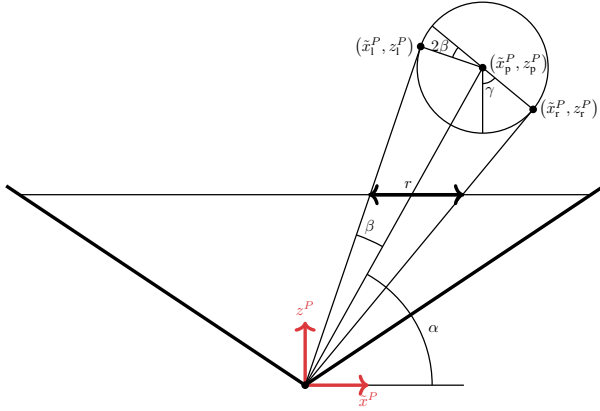
The orientation of the ellipse on the image plane is fully determined by the horizontal position of the particle, and can therefore be computed trivially as:

$$\omega = \arctan 2(y_p^P, x_p^P). \quad (13)$$

Additionally, the center of the ellipse can be computed by observing that (u_r, v_r) and (u_l, v_l) correspond to the



(a) Projection of a sphere onto the image plane



(b) 2D view of the projection of a sphere

Fig. 4: The figures show that the projection of a sphere corresponds to an ellipse (see (a)) in the image plane. The length r of the major axis of this ellipse can be computed via 2D geometry in the plane that contains the optical axis and the ray passing through the camera and the center of the sphere.

projection of (\tilde{x}_r^P, z_r^P) and (\tilde{x}_l^P, z_l^P) , respectively, onto the image plane:

$$x_r^P = \tilde{x}_r^P \cos \omega, \quad y_r^P = \tilde{x}_r^P \sin \omega, \quad (14)$$

$$u_r = f \frac{x_r^P}{z_r^P} + u_0, \quad v_r = f \frac{y_r^P}{z_r^P} + v_0, \quad (15)$$

$$x_l^P = \tilde{x}_l^P \cos \omega, \quad y_l^P = \tilde{x}_l^P \sin \omega, \quad (16)$$

$$u_l = f \frac{x_l^P}{z_l^P} + u_0, \quad v_l = f \frac{y_l^P}{z_l^P} + v_0, \quad (17)$$

where (u_0, v_0) are the coordinates of the pinhole image center.

Therefore, the pixel coordinates of the center are:

$$u_p = \frac{u_r + u_l}{2}, \quad (18)$$

$$v_p = \frac{v_r + v_l}{2}. \quad (19)$$

Finally, noting that the pixel length of the minor axis of the ellipses does not vary with the horizontal coordinates of the sphere [28], this length can be computed for a trivial case, that is, when the center of a particle lies on the optical axis (i.e., $x_p^P = y_p^P = 0$). The same formulas as in (4)-(12) can be employed, since for this special case the projection results in a circle, where both the major axis and the minor axis of the ellipse correspond to the diameter. Using the center, the axis lengths and the orientation of each ellipse, these can be drawn using the drawing functionality of OpenCV¹.

For each indentation step, one image at rest (projecting all the particles, i.e., by setting $s_p^P = s_j^P$ for the j -th particle) and one image after deformation (setting $s_p^P = s_j^P + \Delta s_j^P$ for the j -th particle) were generated. The images were initialized with black pixels, and each ellipse was drawn with a random RGB color to perturb the data with additional variability. The images were then converted to grayscale in a second step. An example of a simulated image is shown in Fig. 1(c). In order to further increase the training robustness, the number of the particles within the gel was slightly perturbed at each indentation step. Training features were then extracted from the images via two different methods:

- 1) Optical flow features: For each indentation step, the dense optical flow between the image at rest and the image after deformation was computed using an algorithm based on Dense Inverse Search [29]. The per-pixel flow was then subsampled performing an average pooling in a grid of 88×88 bins. The two Cartesian components of the optical flow resulted in two matrices, which were concatenated into a two-channel matrix. This method differs from previous work [3], where optical flow features were directly computed from the FEM displacement field, assuming that the density of the particles remained constant during an indentation. In reality, this is not the case for large indentations, as the particles tend to spread radially under pressure, and the method presented here can cope with such conditions.
- 2) Raw features: The two images for each indentation step were subsampled to 88×88 pixels and concatenated into a two-channel image, which was directly fed to the training algorithm.

B. Training labels

The same set of labels described in the following was assigned to each set of features to compose two separate training datasets. For each indentation step, the FEM simulations provide the three-dimensional contact force distribution at the surface nodes of the FEM mesh. Dividing the surface into a grid of 20×20 bins [16], the force components at the nodes falling inside a bin were summed to obtain a 20×20 three-channel matrix, representing the training label for the corresponding indentation step datapoint. Examples of ground truth labels are shown in Fig. 10. In this work, a node was assigned to a certain bin depending on its

¹<https://opencv.org/>

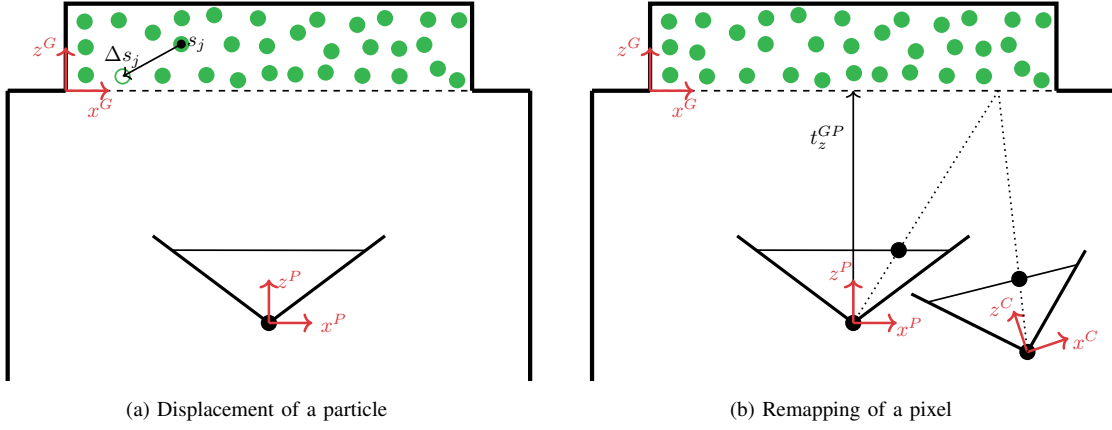


Fig. 5: The drawings show the definition of the three coordinate systems used throughout the article: the gel coordinate system (superscript G), the pinhole camera coordinate system (superscript P), and the real-world camera coordinate system (superscript C). In (a), an example of 3D displacement of a particle originally placed at s_j is depicted. In (b), a pixel in the pinhole camera is mapped to the corresponding pixel in the real-world camera.

initial position before deformation, in order to simplify the binning at the boundaries of the gel, which can vary with deformation. As an alternative, it would also be possible to assign the nodes to the bins according to the position after deformation, by introducing an adaptive binning strategy at the boundaries of the grid.

C. Test dataset

In order to evaluate the real-world performance of the models described in Section IV, 700 test datapoints were collected in an experimental setup, using a programmable milling machine (Fehlmann PICOMAX 56 TOP) to make vertical indentations with the six black indenters shown in Fig. 3. During this procedure, the images taken by the real-world camera were recorded. Since the models were trained with features obtained from images generated via a pinhole camera projection, a further procedure was needed to account for the camera's non-idealities on real-world images [3]. This procedure is denoted as remapping and it essentially maps the pixels from a real-world image (converted to grayscale) to the pixels of an image of the same scene as if it was taken from the ideal pinhole camera used for the training dataset. The remapping procedure requires two main steps:

- 1) Calibration step: during fabrication, seven images of a grid pattern were shot through a silicone medium, see Fig. 6. In this way, it is possible to account for the refractive index of the soft materials. Using a fisheye camera calibration toolbox [30], the images were used to obtain both the extrinsic parameters R^{GC} and t^{GC} of the real-world camera as well as a transformation function from the actual camera 3D coordinate system to the real-world image. The extraction of the extrinsic parameters was achieved by providing the calibration toolbox with a calibration image where the origin of the grid pattern coincided with the origin of the gel coordinate system.
- 2) Interpolation step: for each pixel in the fictitious pinhole image, the corresponding pixel in the real-

world image was obtained, via a procedure sketched in Fig. 5(b). For this step, the pixels were assumed to be placed approximately at a fixed z coordinate in the pinhole camera coordinate system, set here with the bottom of the gel layer. For a pixel $p := (u, v)$ in the image plane of the pinhole camera, a 3D point $s^P := (x^P, y^P, t_z^{GP})$ was retrieved using the pinhole projection equations as:

$$x^P = \frac{t_z^{GP}}{f}(u - u_0), \quad (20)$$

$$y^P = \frac{t_z^{GP}}{f}(v - v_0). \quad (21)$$

The 3D point was then converted to the coordinate system of the real-world camera, indicated with the superscript C , through the corresponding rotation and translation operations:

$$s^C = R^{GC} (R^{GP})^{-1} (s^P - t^{GP}) + t^{GC}. \quad (22)$$

The corresponding pixel in the real-world image was then retrieved via the transformation function obtained from the calibration toolbox. As shown in Fig. 5(b), the approximation introduced above has a smaller effect when the pinhole extrinsic parameters R^{GP} and t^{GP} are close to R^{GC} and t^{GC} , respectively. As mentioned in Section III-A, since the pinhole extrinsic parameters can be set arbitrarily, these were indeed chosen to be close to the expected real-world extrinsic parameters to limit the impact of the approximation. While the calibration parameters are fixed across images of the same camera and can be computed offline, the interpolation step needs to be performed for each image.

The extrinsic parameters obtained during calibration are very sensitive to the exact placement of the grid pattern for the corresponding calibration image. This requires pressing the grid pattern against the silicone medium just enough to remove the air in the middle without penetrating the soft material, which is challenging to achieve in reality.

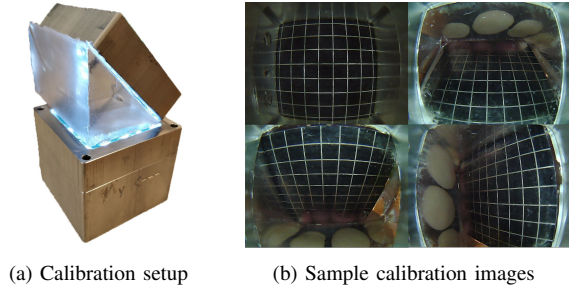


Fig. 6: The calibration images, examples of which are shown in (b), were shot through a silicone medium during fabrication, in order to account for the refraction index of the soft materials. As shown in (a), this was done straight after casting the first layer, by placing additional silicone parts between the first layer and a grid pattern attached to an aluminum surface.

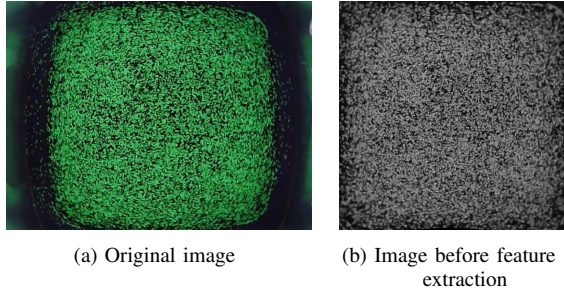


Fig. 7: The original image taken from the real-world camera, shown in (a), was converted to grayscale and remapped as if it was taken from the ideal pinhole camera. A refinement procedure was applied to account for inaccuracies introduced during calibration. The resulting image in (b) shows the particle layer in its actual squared geometry, covering the entire image frame.

Therefore, a grid search (in the sub-millimeter range) was performed in the vicinity of the translation vector t^{GC} , in order to make the particles in a sample remapped image taken at rest match the entire image frame. For this, after a series of dilation and erosion steps, a bounding box around the pixels can be easily computed using OpenCV and compared to the frame boundaries. A refined, remapped image is shown in Fig. 7, where lens distortion effects and misalignments were successfully compensated for.

After remapping, the same image features described in Section III-A were extracted from the images. Since no real-world sensor can provide ground truth contact force distributions, these were extracted in simulation as described in Section III-B and in previous work [16], and assigned to the corresponding features to compose two test datasets. Note that since the real-world camera non-idealities can be compensated in the remapping step, which does not affect training, this enables the transfer of models trained on the pinhole data across multiple instances of fabricated sensors, provided that the camera calibration is performed as described above.

IV. LEARNING ARCHITECTURE

The same learning architecture was employed for both training datasets, that is, on those containing optical flow features and raw features, respectively. The architecture consists of a convolutional neural network, designed as a lightweight

version of u-net [4], and tailored to the estimation of the force distribution from tactile features. In fact, this estimation problem can be formulated as an image-to-image translation [31] (known also as pixel-wise regression). A sketch of the architecture is shown in Fig. 8. The neural network exhibits an encoder-decoder structure, where feature information is first increased in the contraction step by doubling the channels between each pooling operation. In the decoding step, the force distribution is then computed through upconvolutions and concatenations of high-resolution features extracted during the contraction step. As a result, the architecture has the effect of both capturing context and enabling precise localization.

V. RESULTS

The learning architecture was trained twice from scratch using I) the training dataset comprising averaged optical flow features and discretized force distribution labels, and II) the training dataset comprising raw image features and discretized force distribution labels. Both datasets were generated entirely in simulation and both sets of training features contained two-channel 88×88 matrices (or images), as described in Section III-A. The architecture was trained with the AdamW optimizer [32] by minimizing a mean-squared loss with a learning rate of $1e-3$ and a batch size of 256. During training, the datasets were randomly augmented by appropriately flipping the features and labels, exploiting the symmetry of the gel geometry and the pinhole camera projection. For the raw-feature dataset, the images were additionally augmented by perturbing the image brightness and adding salt-and-pepper noise.

After training in PyTorch², the models were converted to the ONNX format, and used in real-time via the ONNX Runtime framework³. This generally led to a 4x inference speed-up on the CPU of a standard laptop (dual-core, 2.80 GHz), compared to the inference in PyTorch.

The performance of both trained models was evaluated on the corresponding synthetic validation datasets, picked randomly as the 20% of the indentation trajectories in the appropriate training dataset. Additionally, the models were evaluated on the corresponding real-world test dataset described in Section III-C. Table I summarizes the results based on two different error metrics for each force component: I) RMSE, that is the root-mean-squared error on the respective component of the force distribution, II) RMSET, that is the root-mean squared error on the respective component of the total force, which was obtained by summing the force distribution over all the bins. The range of total forces in the corresponding dataset is also shown in the table. Note that the vertical indentations performed for the test dataset (spanning vertical forces up to 4.5 N) cause nonzero shear forces due to friction and can cause nonzero horizontal total forces, as the indentations are asymmetrical close to the boundaries of the gel, which are also stiffer due to the black

²<https://pytorch.org/>

³<https://www.onnxruntime.ai/>

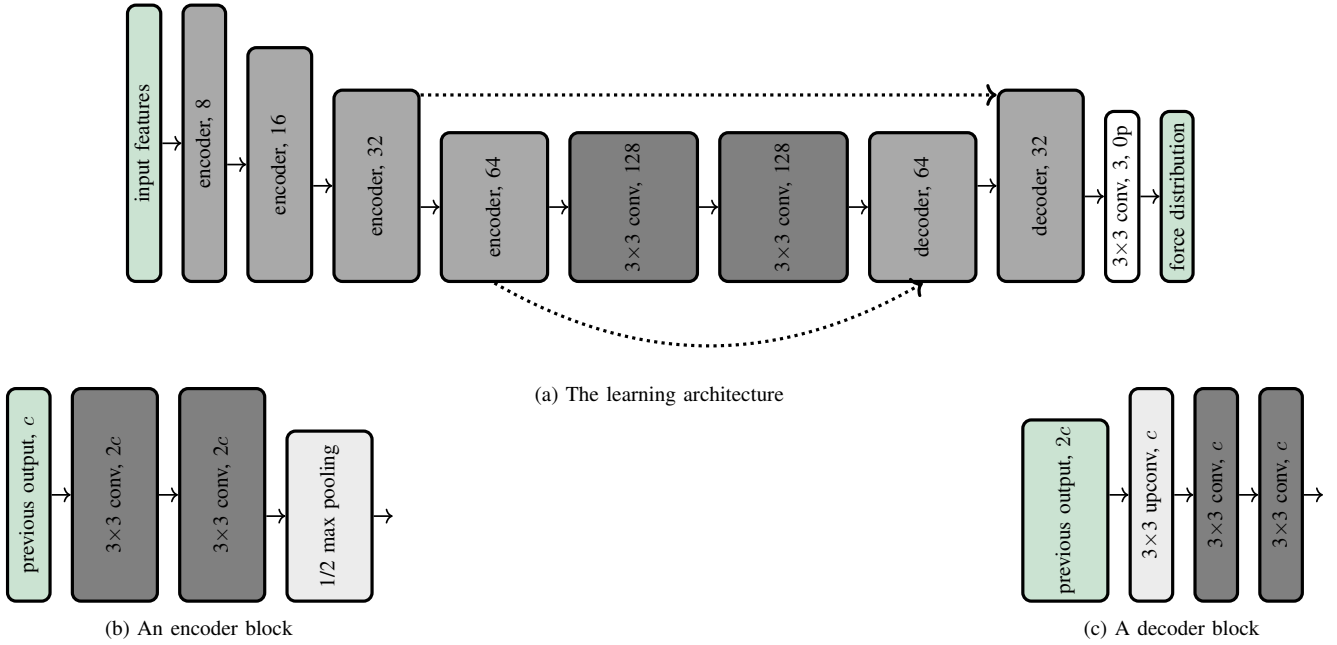


Fig. 8: In (a), a diagram of the learning architecture is shown. The encoder and decoder blocks are summarized in (b) and (c), respectively. All the blocks in green serve as placeholders. “ 3×3 conv, c ” indicates a convolutional layer with a 3×3 filter size and c output channels, while “ 3×3 upconv, c ” indicates an upconvolution that doubles the input size. The dotted lines (omitted in (b) and (c)) indicate the concatenation of an earlier layer output with upsampled information. After each convolutional layer, with the exception of the white one before the final output, batch normalization and rectified linear units were employed. “Op” indicates no padding. Where not indicated, all convolutional filters have unit zero-padding and unit stride.

Elastosil material. Additionally, a contact condition where shear forces are predominant was qualitatively evaluated as shown in Fig. 9(a)-(b).

As the numerical results indicate, the raw-feature model outperformed the optical-flow model in all metrics on the corresponding real-world test dataset. In fact, while in practice the location accuracy for both models was similar, the optical-flow features tend to mitigate the differences across indenters under real-world noise, therefore resulting in inaccurate force predictions. On the other hand, the raw-feature model showed a better transfer from simulation to reality, retaining higher accuracy for all components. In addition to the difference in accuracy, the model trained on the raw image features does not require the extraction of the optical flow, which was the bottleneck for the model trained on optical flow features. As a result, since the model inference only takes about two milliseconds, the whole raw-feature pipeline (including the image acquisition and remapping) runs in real-time at 120 Hz on CPU, compared to the 50 Hz of the optical-flow pipeline.

Examples of the estimation of the force distributions with the model trained on raw features are shown in Fig. 10. The real-time performance of the raw-feature pipeline is shown in the video attached to the article, where contact conditions with arbitrary objects were explored.

VI. CONCLUSION

This work has discussed strategies to simulate the images captured by a vision-based tactile sensor. Starting from FEM simulations, the displacement field was processed to generate training features for a supervised learning architecture that

mapped these features to contact force distribution labels. The resulting models are directly transferable across multiple instances of real-world sensors, since the training procedure does not make use of real-world images. Two different strategies were compared, with the model obtained from raw features outperforming a model based on optical flow features for both real-world accuracy and inference speed. In addition to providing a physical quantity directly interpretable across robotic tasks, the extraction of accurate force distributions also provides an abstraction from the image pixels that bypasses the remaining mismatch between real and simulated images.

Since this work aimed to provide a comparison between the two approaches, the same input and output sizes were employed for both strategies. However, given the gain in prediction speed, the raw-feature approach may be extended to use higher-resolution features or to predict the force distribution on a finer grid by trading off the sensing frequency. As shown in Table I, a gap still remains between simulation and reality, which could be addressed by explicitly addressing the domain transfer problem. This issue will be the subject of future work.

ACKNOWLEDGEMENTS

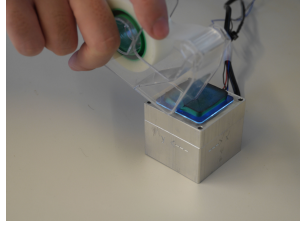
The authors would like to thank Michael Egli for his support in the sensor manufacture, and Thomas Bi for the discussions on the sensing pipeline.

REFERENCES

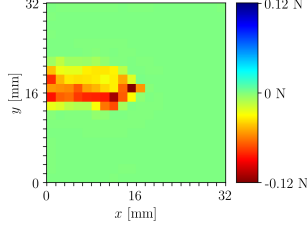
- [1] C. Sferrazza and R. D’Andrea, “Design, Motivation and Evaluation of a Full-Resolution Optical Tactile Sensor,” *Sensors*, vol. 19, no. 4:928, 2019.

	RMSE [N]			RMSET [N]			Range of total forces [N]		
	x	y	z	x	y	z	x	y	z
Optical-flow (sim)	0.004	0.004	0.010	0.072	0.078	0.266	-4.0 – 4.0	-4.0 – 4.0	-12.0 – 0
Raw-feature (sim)	0.004	0.004	0.010	0.093	0.091	0.218	-4.0 – 4.0	-4.0 – 4.0	-12.0 – 0
Optical-flow (real)	0.004	0.005	0.017	0.144	0.149	0.900	-0.2 – 0.2	-0.5 – 0.5	-4.5 – 0
Raw-feature (real)	0.003	0.004	0.011	0.043	0.038	0.281	-0.2 – 0.2	-0.5 – 0.5	-4.5 – 0

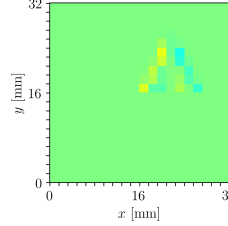
TABLE I: The table shows the error metrics of the trained models on the validation datasets extracted in simulation and the test datasets collected in reality, for both the cases where optical flow features and raw features are used as inputs.



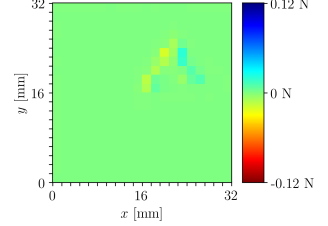
(a) Indentation inducing high shear forces



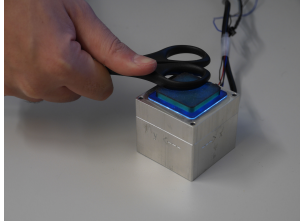
(b) Prediction - y component



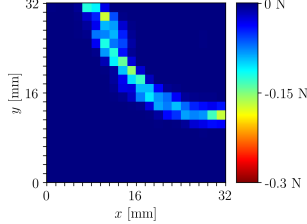
(a) Ground truth - x component



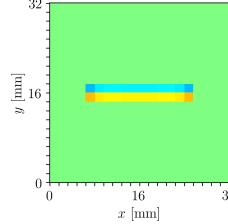
(b) Prediction - x component



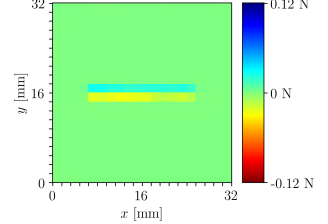
(c) Indentation with scissors



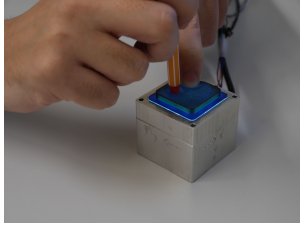
(d) Prediction - z component



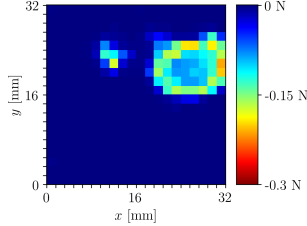
(c) Ground truth - y component



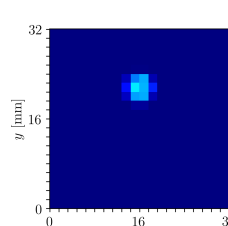
(d) Prediction - y component



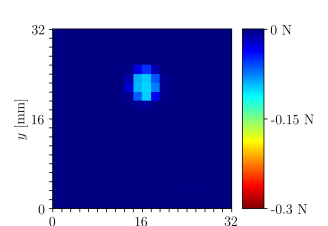
(e) Indentation with multiple contacts



(f) Prediction - z component



(e) Ground truth - z component



(f) Prediction - z component

Fig. 9: The figures show sensible predictions for different contact conditions. In (a)-(b), the tape dispenser was first pressed against the gel and then translated to induce higher forces in the negative y direction. In (c)-(d) the contact with an object of unknown geometry is shown, while (e)-(f) show the contact with multiple bodies (not included in the training data) with different shape and applied pressure.

Fig. 10: The plots show the ground truth and predicted force distribution components for different samples in the real-world test dataset. Predictions were made with the raw-feature model. (a)-(b) show an indentation with a flat triangular indenter, (c)-(d) with a cylindrical indenter, and (e)-(f) with a spherical indenter.

[2] D. V. Hutton, *Fundamentals of Finite Element Analysis*. McGraw-Hill, 2004.

[3] C. Sferrazza, T. Bi, and R. D'Andrea, "Learning the sense of touch in simulation: a sim-to-real strategy for vision-based tactile sensing," in *Proceedings of the IEEE International Conference on Intelligent Robots and Systems*, 2020.

[4] O. Ronneberger, P. Fischer, and T. Brox, "U-Net: Convolutional Networks for Biomedical Image Segmentation," in *Proceedings of the International Conference on Medical Image Computing and Computer-Assisted Intervention*, pp. 234–241, 2015.

[5] R. S. Dahiya, G. Metta, M. Valle, and G. Sandini, "Tactile Sensing—From Humans to Humanoids," *IEEE Transactions on Robotics*, vol. 26, no. 1, pp. 1–20, 2010.

[6] K. Shimonomura, "Tactile Image Sensors Employing Camera: A Review," *Sensors*, vol. 19, no. 18:3933, 2019.

[7] B. Ward-Cherrier, N. Pestell, L. Cramphorn, B. Winstone, M. E. Giannaccini, J. Rossiter, and N. F. Lepora, "The TacTip Family: Soft Optical Tactile Sensors with 3D-Printed Biomimetic Morphologies,"

Soft robotics, vol. 5, no. 2, pp. 216–227, 2018.

[8] F. Baghaei Naeini, D. Makris, D. Gan, and Y. Zweiri, "Dynamic-Vision-Based Force Measurements Using Convolutional Recurrent Neural Networks," *Sensors*, vol. 20, no. 16:4469, 2020.

[9] A. C. Abad and A. Ranasinghe, "Visuotactile Sensors with Emphasis on GelSight Sensor: A Review," *IEEE Sensors Journal*, vol. 20, no. 14, pp. 7628–7638, 2020.

[10] C. Trueeb, C. Sferrazza, and R. D'Andrea, "Towards vision-based robotic skins: a data-driven, multi-camera tactile sensor," in *Proceedings of the IEEE International Conference on Soft Robotics*, pp. 333–338, 2020.

[11] M. Lambeta, P.-W. Chou, S. Tian, B. Yang, B. Maloon, V. R. Most, D. Stroud, R. Santos, A. Byagowi, G. Kammerer, D. Jayaraman, and R. Calandra, "DIGIT: A Novel Design for a Low-Cost Compact High-Resolution Tactile Sensor With Application to In-Hand Manipulation," *IEEE Robotics and Automation Letters*, vol. 5, no. 3, pp. 3838–3845, 2020.

[12] A. Padmanabha, F. Ebert, S. Tian, R. Calandra, C. Finn, and S. Levine,

- "OmniTact: A Multi-Directional High Resolution Touch Sensor," in *Proceedings of the IEEE International Conference on Robotics and Automation*, pp. 618–624, 2020.
- [13] E. Donlon, S. Dong, M. Liu, J. Li, E. Adelson, and A. Rodriguez, "GelSlim: A High-Resolution, Compact, Robust, and Calibrated Tactile-sensing Finger," in *Proceedings of the IEEE/RSJ International Conference on Intelligent Robots and Systems*, pp. 1927–1934, 2018.
- [14] D. Ma, E. Donlon, S. Dong, and A. Rodriguez, "Dense Tactile Force Estimation using GelSlim and inverse FEM," in *Proceedings of the IEEE International Conference on Robotics and Automation*, pp. 5418–5424, 2019.
- [15] N. Kuppuswamy, A. Castro, C. Phillips-Grafflin, A. Alspach, and R. Tedrake, "Fast Model-Based Contact Patch and Pose Estimation for Highly Deformable Dense-Geometry Tactile Sensors," *IEEE Robotics and Automation Letters*, vol. 5, no. 2, pp. 1811–1818, 2019.
- [16] C. Sferrazza, A. Wahlsten, C. Trueeb, and R. D'Andrea, "Ground Truth Force Distribution for Learning-Based Tactile Sensing: A Finite Element Approach," *IEEE Access*, vol. 7, pp. 173438–173449, 2019.
- [17] W. Yuan, S. Dong, and E. H. Adelson, "GelSight: High-Resolution Robot Tactile Sensors for Estimating Geometry and Force," *Sensors*, vol. 17, no. 12: 2762, 2017.
- [18] P. Piacenza, K. Behrman, B. Schifferer, I. Kymissis, and M. Ciocarlie, "A Sensorized Multicurved Robot Finger With Data-Driven Touch Sensing via Overlapping Light Signals," *IEEE/ASME Transactions on Mechatronics*, vol. 25, no. 5, pp. 2416–2427, 2020.
- [19] Y. S. Narang, K. Van Wyk, A. Mousavian, and D. Fox, "Interpreting and Predicting Tactile Signals via a Physics-Based and Data-Driven Framework," in *Proceedings of Robotics: Science and Systems*, 2020.
- [20] H. Lee, H. Park, G. Serhat, H. Sun, and K. J. Kuchenbecker, "Calibrating a Soft ERT-Based Tactile Sensor with a Multiphysics Model and Sim-to-real Transfer Learning," in *2020 IEEE International Conference on Robotics and Automation*, pp. 1632–1638, 2020.
- [21] Z. Ding, N. F. Lepora, and E. Johns, "Sim-to-Real Transfer for Optical Tactile Sensing," in *Proceedings of the IEEE International Conference on Robotics and Automation*, pp. 1639–1645, 2020.
- [22] D. F. Gomes, A. Wilson, and S. Luo, "GelSight Simulation for Sim2Real Learning," in *ICRA ViTac Workshop*, 2019.
- [23] Y. Wang, W. Huang, B. Fang, and F. Sun, "Elastic Interaction of Particles for Robotic Tactile Simulation," *arXiv preprint arXiv:2011.11528*, 2020.
- [24] R. W. Ogden, "Large deformation isotropic elasticity – on the correlation of theory and experiment for incompressible rubberlike solids," in *Proceedings of the Royal Society of London. A. Mathematical, Physical and Engineering Sciences*, vol. 326, pp. 565–584, 1972.
- [25] M. Ciavarella, D. Hills, and G. Monno, "The influence of rounded edges on indentation by a flat punch," *Proceedings of the Institution of Mechanical Engineers, Part C: Journal of Mechanical Engineering Science*, vol. 212, no. 4, pp. 319–327, 1998.
- [26] L. Mitas and H. Mitasova, "Spatial interpolation," in *Geographical Information Systems: Principles, Techniques, Management and Applications* (P. A. Longley, M. F. Goodchild, D. J. Maguire, and D. W. Rhind, eds.), John Wiley & Sons, 1999.
- [27] R. Szeliski, *Computer Vision: Algorithms and Applications*. Springer, 2010.
- [28] D. S. Wokes and P. L. Palmer, "Perspective Projection Of A Spheroid Onto An Image Plane," *SIAM Journal of Imaging Sciences*, 2008.
- [29] T. Kroeger, R. Timofte, D. Dai, and L. Van Gool, "Fast Optical Flow using Dense Inverse Search," in *Proceedings of the European Conference on Computer Vision*, pp. 471–488, 2016.
- [30] D. Scaramuzza, A. Martinelli, and R. Siegwart, "A Toolbox for Easily Calibrating Omnidirectional Cameras," in *Proceedings of the IEEE/RSJ International Conference on Intelligent Robots and Systems*, pp. 5695–5701, 2006.
- [31] S. Kaji and S. Kida, "Overview of image-to-image translation by use of deep neural networks: denoising, super-resolution, modality conversion, and reconstruction in medical imaging," *Radiological Physics and Technology*, vol. 12, no. 3, pp. 235–248, 2019.
- [32] I. Loshchilov and F. Hutter, "Decoupled Weight Decay Regularization," in *Proceedings of the International Conference on Learning Representations*, 2019.